Computational methods in wind power meteorology

Jørgensen, Bo Hoffmann; Ott, Søren; Sørensen, Niels N.; Mann, Jakob; Badger, Jake

Publication date:
2007

Document Version
Publisher's PDF, also known as Version of record

Risø-R-Report

Computational methods in wind power meteorology

Bo Hoffmann Jørgensen, Søren Ott, Niels Nørmark Sørensen, Jakob Mann and Jake Badger

Risø–R–1560(EN)

Risø National Laboratory
Technical University of Denmark
Roskilde, Denmark
June 2007

Author: Bo Hoffmann Jørgensen, Søren Ott, Niels Nørmark Sørensen, Jakob Mann and Jake Badger
Title: Computational methods in wind power meteorology
Department: Wind Energy Department

Risø–R–1560(EN)
June 2007

Abstract (max. 2000 char.):

Subsets of measured wind data from the Hjardemål field experiment are extracted in order to produce test cases representing nearly stationary, neutral conditions with well defined upstream flow. Model solutions of the Reynolds Averaged Navier-Stokes (RANS) equations are obtained by utilizing the numerical flow solver EllipSys3D. When utilizing the well-known k-epsilon model as a turbulence closure, the result is a nearly complete agreement between the measurements and the model solution - not only for the forward flow but also for the separating backward flow over the Hjardemål escarpment. Small deviations can be understood from analyzing the conditions of the field experiment. It is of vital importance to understand the conditions under which the flow solver yields accurate solutions, in particular with respect to the grid generation, which was performed with the hyperbolic grid generator HypGrid2D/3D. The grid must allow the model to represent the underlying physics of the flow problem and the grid resolution must be sufficient to produce grid independent solutions. This yields not only the correct mean velocity but also the correct Turbulent Kinetic Energy (TKE). Deviations of the TKE in the zone very close to onset of separation might be understood by addressing the assumptions of a zero horizontal pressure gradient in the momentum balance near the surface. It is argued on basis of the obtained results that the model can be extended to non-neutral conditions and more complex terrain. The difficulties in using existing measurement data from a sparsely instrumented site, Porto, in complex terrain in Portugal for evaluating the model are demonstrated. Suggestions are offered to assist future field work incorporating wind measurements for complex terrain and non-neutral conditions in order to evaluate numerical flow models.

ISSN 0106-2840
ISBN 87-550-3522-1

Contract no.:

Group's own reg. no.:

Sponsorship:

Cover :

Pages:
Tables:
References:

Information Service Department
Risø National Laboratory
Technical University of Denmark
P.O.Box 49
DK-4000 Roskilde
Denmark
Telephone +45 46774004
bibl@risoe.dk
Fax +45 46774013
www.risoe.dk

Contents

1 Introduction

This report has been prepared in connection with the project called Computational methods in wind power meteorology which was supported by the Danish Technical Research Council (STVF). The report is concerned with the treatment of measurement data for the full scale atmospheric test sites Hjardemål and Porto, and the associated RANS-calculations utilizing the $k-\varepsilon$ turbulence model. Other reports in preparation describe the work with grid generation and very complex terrain. Also, a report in preparation by Lisbeth Myllerup describes the work with non-linear two-equation turbulence models. The work on Detached Eddy Simultaion (DES) is presented in the PhD Thesis by Andreas Bechmann (Bechmann 2007).

In 2003, we engaged in interdisciplinary research between the Meteorology programme (MET) and the Aeroelasticity programme (AED) of the Wind Energy Department to produce accurate characteristics of unsteady wind fields necessary to predict the dynamic loads on engineering structures. Also, this approach was expected to enable a better estimate of the mean wind field. We have combined our knowledge of atmospheric modelling and the computation of aerodynamical flows in order to compute atmospheric flows in complex terrain with greater accuracy in the lowest part of the atmosphere where most man made structures reside. On the microscale in very complex terrain, we employed methods of Computational Fluid Dynamics (CFD) by utilizing our existing state-of-the-art CFD model EllipSys3D. This model was developed in collaboration with the Technical University of Denmark (DTU), see Michelsen (1992), Michelsen (1994) and Sørensen (1995). The model has been enhanced with new boundary conditions, atmospheric driving forces and new sophisticated turbulence models. Furthermore, the model has been tested against realistic test cases for atmospheric flow over natural terrain as well as more detailed wind tunnel test cases.

The background for the present report is a desire to test the ability of the Reynolds Averegaged Navier-Stokes (RANS) equations utilized in conjunction with a $k-\varepsilon$ turbulence model to simulate the atmospheric flow over terrain. This has previously been a subject for studies in connection with the Askervein Hill, see for instance Castro, Palma and Lopes (2003) but also for a few other sites such as in Kim and Patel (2000). The Askervein Hill has been the subject of a several studies based on measuremens such as in Walmsley and Taylor (1996) and Taylor and Teunissen (1987). There is in general a lack of appropriate experimental test cases for verification of CFD models of atmospheric flow over natural terrain. In the present report, we focus on the two other sites which have previously been studied via measurements of Risø National Laboratory.

2 Test cases for flow modelling over complex terrain

2.1 Hjardemål

Background

The site and the instrumentation is described in detail in the 'official' data report Emeis, Courtney, Højstrup and Jensen (1993).

The Hjardemål experiment was conducted in September and October 1989 at a site near Hjardemål in Northern Jutland. The site is generally flat rural terrain except for an escarpment that cuts through the landscape. The escarpment was formed during the last glaciation where it marked the coastline. It is shaped as a 30^{o} ramp raising about 16 m from the old, flat sea floor to a wide plateau, which is almost as flat. At the place where the

experiment was conducted the escarpment is almost linear running approximately NW to SE (332°).

The experiment was conducted shortly after the fields had been harvested, but not yet ploughed, hence the soil was mostly bare. Hedges on the low side of the escarpment running along 236°, divide the landscape into long strips of fields for different use. The mast array was placed midway between two of these hedges with 40 m distance to either of the hedges. Thus the array was oriented along 236°, which is close to being perpendicular to the escarpment (242°). From a photo the southern hedge appears to be about 5 m high consisting of a single, largely transparent row of small trees with few leaves. The northern hedge appears to a 1 m high stone fence with little vegetation on it and can perhaps be ignored. It should be noted that figure 2.1 of the data report is not consistent with the photos regarding the length of the southern hedge. According to the photos it extends beyond the canal and according to Niels Otto Jensen, who participated in the measurements, it extended far beyond Hunstrup Å. This is confirmed by a map made by Kort- og Matrikelstyrelsen which shows hedges in the area. A photo showing the hedges viewed from the top of the escarpment would have been helpful, but does not seem to exist. Figure 2.1 of the data report also shows a hedge on the high side of the escarpment directed approximately along 206°. This hedge, which was about 3–4 m high and dense, was located about 60 m from the array at the closest point (at the edge of the escarpment). The 4 m high hedges could seriously affect the measurements except (perhaps) for wind directions very close to 236° or to the opposite direction 56°. In the intervals $229-247^{\circ}$ and $47-64^{\circ}$ none of the mast are placed directly downwind any part of the hedges. A wind turbine was situated in the hedge on the high side about 100 m away from the mast array.

Data was recorded by three computers and stored on tapes. There has been some unfortunate difficulties reading these tapes. The tape recorder had to be repaired, but some of the tapes were still unreadable because of mechanical failure of the cartridges (the tape itself could be ok). Although most of the data has been saved, runs 44 and 45 seem to be lost.

A PC program was made to facilitate data browsing. Using the program periods of stationary meteorological conditions for at leat 30 minutes, favorable wind directions and neutral stability were selected. In this way six cases could be defined. Four of the cases are up–slope while two are down–slope. Table 1 shows some key data.

Atmospheric stability was measured both by sonic anemometers (of various kinds) and by temperature difference measurements on Mast 1 (the reference mast placed 400 m upwind of the escarpment). The Monin–Obukhov length scale (L) measured by a sonic is listed in Table 1. The ratio z/L appears in expressions for Monin–Obukhov similarity profiles and can be regarded as a measure of atmospheric stability. Except for run 18, which is the most stable run, large (positive or negative) values of L are found. This signalizes nearly neutral conditions where $L \to \pm\infty$. The values are given as intervals because of large fluctuations. Similar measurements at the 25 m level (not shown) are only roughly consistent with those at 10 m. Such discrepancies are to be expected for near neutral conditions where L is difficult to measure due to the low heat flux. It therefore does not seem appropriate to use these measurements for more than a qualitative consistency check. Profiles from Mast 1 could also be used to judge stability, but interference from the hedges makes it difficult to establish the upstream temperature and wind profiles except for wind directions very close to 236°. Finally, a stability measure, the bulk Richardson number Ri, can be obtained from the temperature difference measurements and velocity measurements. We have chosen this approach since it seems to the most robust and reliable.

The bulk Richardson number is defined as

$$\mathrm{Ri} = \frac{\Delta\Theta\, g \Delta z}{T(\Delta u)^2} \tag{1}$$

where T is the absolute temperature, g is the acceleration of gravity, $\Delta\Theta$ is the difference

Table 1. Parts of runs with good direction.

run	t_1	t_2	σ_θ	$\langle\theta\rangle$	U	$\frac{\Delta u_b}{u_b-u_a}$	Ri
	[min]	[min]	M1 25 m [deg]	M1 25 m [deg]	M1 10 m [m/s]	[–]	[–]
18	50	110	3	244	4.7	0.06	0.023
22	1	30	5	239	6.9	0.02	0.009
27	45	105	7	64	7.5	-0.04	0.005
28	260	440	7	59	8.0	-0.03	0.003
37	15	45	6	264	6.1	0.01	0.006
37	90	150	7	264	5.7	0.02	0.012

of potential temperatures measured at two heights z_2, $z_1 = z_1 + \Delta z$ and $\Delta u = u(z_2) - u(z_1)$ is the corresponding difference of wind speeds. The potential temperature difference is obtained from the measured temperature difference using the relation

$$\Delta\Theta = \Delta T + \Delta z g/C_p \tag{2}$$

where $g/C_p = 0.0098\mathrm{K/m}$ is the adiabatic lapse rate. Here measurements refer to $z_1 = 2\,\mathrm{m}$ and $z_2 = 23\,\mathrm{m}$ on Mast 1.

Although *Ri* is a convenient measure of effect of stability on the velocity profile in the flat, upwind terrain it does not directly quantify the effect on the speedup. The model doesn't take stability into account, so a rough measure is of interest. To this end we consider the path a fluid element starting far away on the downhill side of the escarpment with velocity u_a and ending at the crest with velocity u_b. If the fluid parcel is buoyant with respect to the surrounding fluid it will gain of potential energy equal to $\Delta E_{\mathrm{pot}} = \Delta\rho g H \sim -\rho g H \Delta\Theta/T$, where H is the height of the escarpment, and $\Delta\Theta$ is the difference of potential temperature of the fluid element and that of the ambient. This potential energy is supplied by the flow and, as a worst case, we may simply subtract it from the kinetic energy $E_{\mathrm{kin}} = \frac{1}{2}\rho u_b^2$ of the fluid element. The change of u_b caused by stability can therefore be evaluated as $\Delta u_b = \Delta E_{\mathrm{pot}}/(\rho u_b)$. Comparing this to the speed up $u_b - u_a$, gives the desired, rough idea of the importance of stability. Table 1 lists the ratio

$$\frac{\Delta u_b}{u_b - u_a} \sim -\frac{\Delta\rho g H}{\rho u_b (u_b - u_a)} \sim \frac{\Delta\Theta g H}{T u_b (u_b - u_a)} \tag{3}$$

For practical purposes we set $u_b = u(2\mathrm{m})$ on mast 7, where the largest speedup is observed, and estimate $\Delta\theta$ from the measurements on mast 1. In all cases the resulting extra speedup caused by stability is only a few percent of the measured $u_b - u_a$ as can be seen from the table. The worst case is run 18, but even here the effect is only 6%. This justifies the neglect of stability effects in calculations.

The upwind profile is an important model input and should be properly specified. The problem is that the reference mast profile might be influenced both by stability and by the fences and possibly also by the presence of the escarpment. The profile of $u(10\,\mathrm{m})$ along the array shown in figure 1 does not become entirely flat at the ends indicating

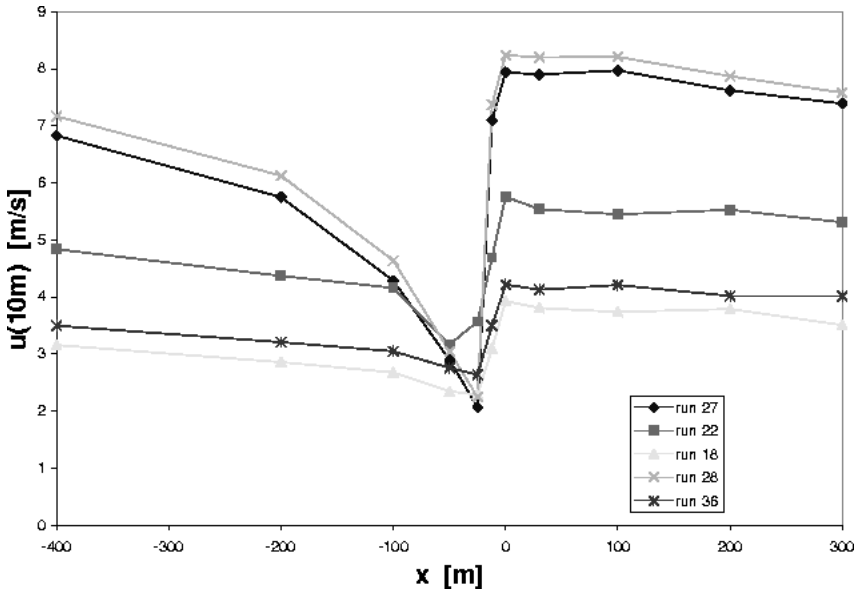

Figure 1. Horizontal u–profiles for cups at 10 m height.

some effect of the escarpment even at the ends. The vertical profile at the reference mast in case of wind parallel to the lower hedge (236°) is not particularly logarithmic and it does not seem possible to separate the influence of stability from the influence of the escarpment. However, 'clean' results are obtained for run 14 where the wind direction is is almost parallel with the scarp (310°) and the wind speed is relatively high. Here the reference mast wind profile is perfectly logarithmic and with $z_0 = 6$ cm. Run 21 (280°) is also useable and yields the same result for z_0. The good fits to logarithmic profiles indicate that the northern fence on the low need not be counted as an individual obstacle, but can blend into the general roughness, which is about 6 cm. We can also infer that the non-logarithmic profiles observed for other directions are not artifacts caused by bad calibrations and that the influence of nearby, upwind hedges is substantial. The best wind direction is therefore one somewhat larger than (236°), but not too large since then the masts on the high side come in the lee of the hedge there.

2.2 Porto

This dataset consists of a anemometer and wind vane measurements from a number of met stations located near Porto in the Northern Portugal. The stations are referred to with numbers, e.g. Station 1, Station 2 etc. Station 1 is located by the sea whereas the rest are located in mountainous, complex terrain. The stations form an east-west band stretching from the coast and some 100 km into the land. The data was used for the European Wind Atlas where brief descriptions of the sites are given. They are mostly located on hilltops in open areas covered with grass and small bushes and without obstacles disturbing the mast.

The data records contain ten minutes averages of wind speed and wind direction along with a ten minutes gust speed, which presumably is just the largest single measurement. Neither turbulence data nor temperatures are available. The data covers a period of about 4 years from 1991 to 1995. Generally the data seem neat and reliable with bad measurements marked by the value 99.99 for wind speeds and 999 for directions.

The distances between the stations are generally larger than optimal for making test cases, but Stations 5,6,7,8,9 and 10 form a more compact group with distances ranging from 2.5 to 12km. These stations were selected for the analysis.

The purpose is to find good test cases for the flow model. Generally, the model assumes neutral, baroclinic condition (no thermal wind) and a homogeneous, stationary forcing by a constant pressure gradient. In reality these conditions are rare, if at all existing. It should be noted that the timescales of the system are long. If we imagine an abrupt change of the pressure gradient from one uniform value to another, which at least is possible in a model context, then the duration of the subsequent transient will be governed by the Coriolis parameter. It would take several days for the flow to adjust to the new forcing. In the atmosphere the forcing cannot be expected to stay constant for so long. We therefore cannot expect to find ideal, stationary conditions for the whole boundary layer. The fact that we are dealing with a coastal region with mountains further complicates matters since the flow will not only be forced by the pressure gradient but also be thermally driven.

We might be able to find approximately homogeneous and stationary conditions for a smaller part of the boundary layer, not necessarily extending all the way to the top but still large enough to cover several stations.

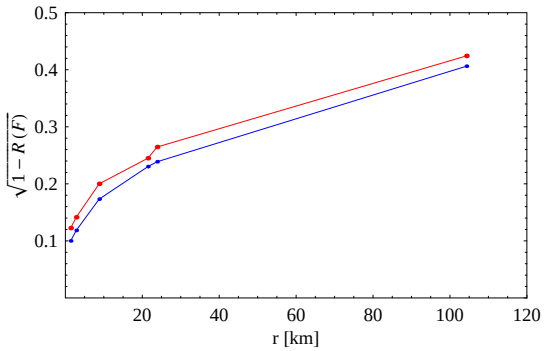

Figure 2. $\sqrt{1-R(F)}$ *vs distance between stations. Data taken from figure 7 in Ayotte* et al. *(1998). Red:* $1/F = 30$ *min. Blue:* $1/F = 2.4$ *hours.*

Ayotte, Davy and Coppin (2001) discuss the problems encountered when comparing models which assume neutral stratification with real world data. The analysis is based on two–point statistics of wind speed and direction measurements taken at met station located in a rolling terrain, and distances between stations range from 1 to 100 kilometers. Among other things they look at the correlation coefficient $R(F)$ for the band–limited wind speeds measured at two stations. The band-limited wind speed is obtained by neglecting all Fourier components with frequencies above a certain limit frequency F. In the time domain this corresponds to a convolution of the signal with $\frac{\sin \pi F t}{\pi t}$, which has quite thick tails (second moment not defined). We may interpret $R(F)$ as a measure of the variance of a common, correlated component of the two *filtered* signals. Likewise $\sqrt{1-R(F)}$ can be interpreted as the ratio of rms amplitudes of the uncorrelated part and the correlated part. Thus $\sqrt{1-R(F)}$ is a measure of the 'error' due to lack of correlation that occurs when the wind speed is transformed from one station to another. It is normalized with respect to the standard deviation for the whole period, in this case one year, which is a bit odd. For a Weibull distribution with $k = 2$ the standard deviation is about half of the mean. Figure 2 shows $\sqrt{1-R(F)}$ vs distance between stations for averaging periods (1/F) equal to 30 minutes and 2.4 hours. These results indicate that parts of the unpredictable component of the wind field resides on quite low frequencies.

The simple, and perhaps naive, picture is that the ten minutes average of the wind speed determines the global forcing, at least when the wind is reasonably steady-state for a somewhat longer period surrounding the ten minutes so that we can rely on the forcing being reasonably constant. Conversely, we may ask what variations of the ten minutes mean we would expect if the forcing was ideally uniform and constant. This would be relevant not only for measured data but also for model simulations where the question is

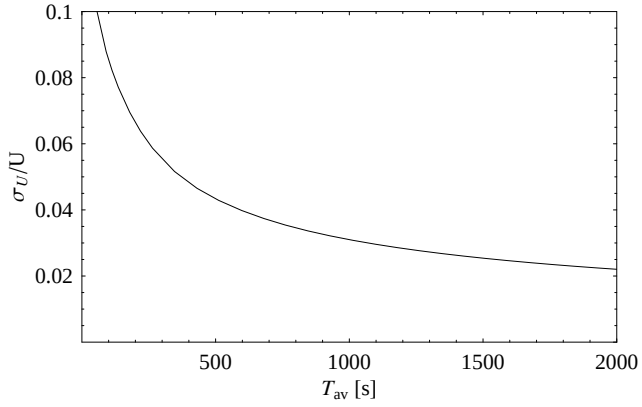

Figure 3. Relative standard deviation of U as a function of averaging time $T_{\rm av}$.

how long the simulation should be in order to capture the long term fluctuations. According to Högström, Hunt and Smedman (2002) (see also Hunt and Morrison 2000) there is a regime in the low frequency part where the spectrum goes as $1/n$, where n is the frequency. They find

$$S_u(n) = \begin{cases} \gamma u_*^2/n_l & \text{if } n < n_l \\ \\ \gamma u_*^2/n & \text{if } n_h > n > n_l \end{cases} \tag{4}$$

where

$$\begin{aligned} \gamma &\approx 1.0 \\ n_l &= \frac{\gamma U f_c}{u_* A} \\ n_h &= \frac{U}{2\pi z} \\ A &\approx 0.2 + 0.047\mathrm{m}^{-1}\, z \end{aligned} \tag{5}$$

and f_c is the Coriolis parameter. For measurements taken at 10 m height with $z_0 = 3$cm we find $n_l = 22 f_c = 2.4\,10^{-3}$ Hz and $n_h = 0.16$ Hz. The lower limit determines the largest relevant time scale $T_{\rm max}$, i.e.

$$T_{\rm max} = \frac{1}{22 f_c} \approx 7 \text{ minutes} \tag{6}$$

It should be noted that such a regime is in fact found in LES simulations so it must be regarded as part of the model prediction. Figure 3 shows the relative standard error of U as a function of the averaging time $T_{\rm av}$. For $T_{\rm av} = 600$ seconds we find a standard error of about 4%. The number is for uniform terrain and it could be larger in complex terrain. In terms of wind direction variability this corresponds to 2.3 degrees. This suggests that constant forcing could be characterized by periods longer than 10 minutes where the ten minutes averaged U stays constant within 4%. If effects of stratification and terrain can be ignored then a scatter plot of simultaneous wind directions measured at two different stations is expected to show a collapse of points in a narrow band about 5 degrees wide. However, such periods are extremely rare. If we demand that σ_U/U<0.04 for a period of one hour then the direction scatter plots contain only a few handfuls of points. Moreover, there is no sign of collapse at all. It therefore seems that the selection is too restrictive and that it might pick out periods with spuriously constant measurements, for example caused by ice temporarily clamping the vanes. Better results are obtained by relaxing the conditions. The following procedure was followed:

- Station 8 was selected as reference station. It is placed central among stations 6–10 and it has good data coverage.

- Records with $U < U_{\min}$=8 m/s or $U > U_{\max}$=20 m/s were deleted. Here U refers to the measurement at the reference station.
- For all stations a long term average $\overrightarrow{U}$ was found by averaging over 150 minutes intervals, i.e n=15 ten minutes readings. $\overrightarrow{U}$ was then used to define the mean wind direction and downwind/crosswind component U and V for each of the n ten minutes recording. From this and standard errors σ_U and σ_V were calculated and data was rejected if $\sigma_U/U > \varepsilon_U = 0.15$ or $\sigma_V/U > \varepsilon_V = 0.15$.
- For each station $\overrightarrow{U}$ was retained if a simultaneous value $\overrightarrow{U}_{\text{ref}}$ was available from the reference station. These pairs were then binned into 72 sectors according to the (150 minutes mean) wind direction at the reference stations. The averages of $\overrightarrow{U}$ and $\overrightarrow{U}_{\text{ref}}$ over a bin was used to define corresponding wind directions and a wind speed ratio $|\overrightarrow{U}|/|\overrightarrow{U}_{\text{ref}}|$ for each sector. Standard errors of these quantities were also calculated.

This selection procedure yields scatter plots with a fairly good collapse of points. Figure 4 shows the scatter plot for Stations 8 and 9 with.

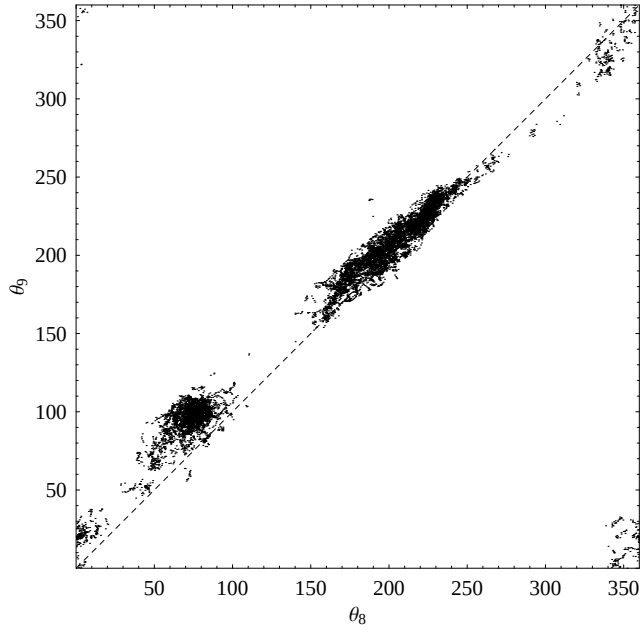

Figure 4. Scatter plot of 150 minutes average wind direction at Stations 8 and 9.

Various other choices of $U_{\min}$, $U_{\max}$, n, ε_U and ε_V were tried. It turns out that results are insensitive, within statistical errors, to changes of $U_{\min}$ and $U_{\max}$ as long as both are larger than 8 m/s. Making n larger or ε_U or ε_V smaller, i.e. being more restrictive with respect to stationarity of the wind, has no effect on the scatter. Only when the selection gets very restrictive we see an *increase* of the scatter.

Figure 5 shows analysed data for Stations 6,7,9 and 10 with Station 8 as reference. The vertical error bars indicate $\pm$one standard deviation which appear to be somewhat larger than expected from the model spectra of Högström and Hunt. The horizontal error bars merely reflect the size of the sectors. Data points are missing for some of the sectors due to lack of data. The wind directions are not dramatically different from the wind direction at the reference station, which might be caused by the fact that all stations are located on hill tops. The wind speed ratios show more variation.

Without any thermal data it is hard to judge the stability. However, stability effects are more pronounced at low wind speeds than at high wind speeds, so a lower bound on the wind speed helps selecting neutral cases. In principle we could eliminate stability effects

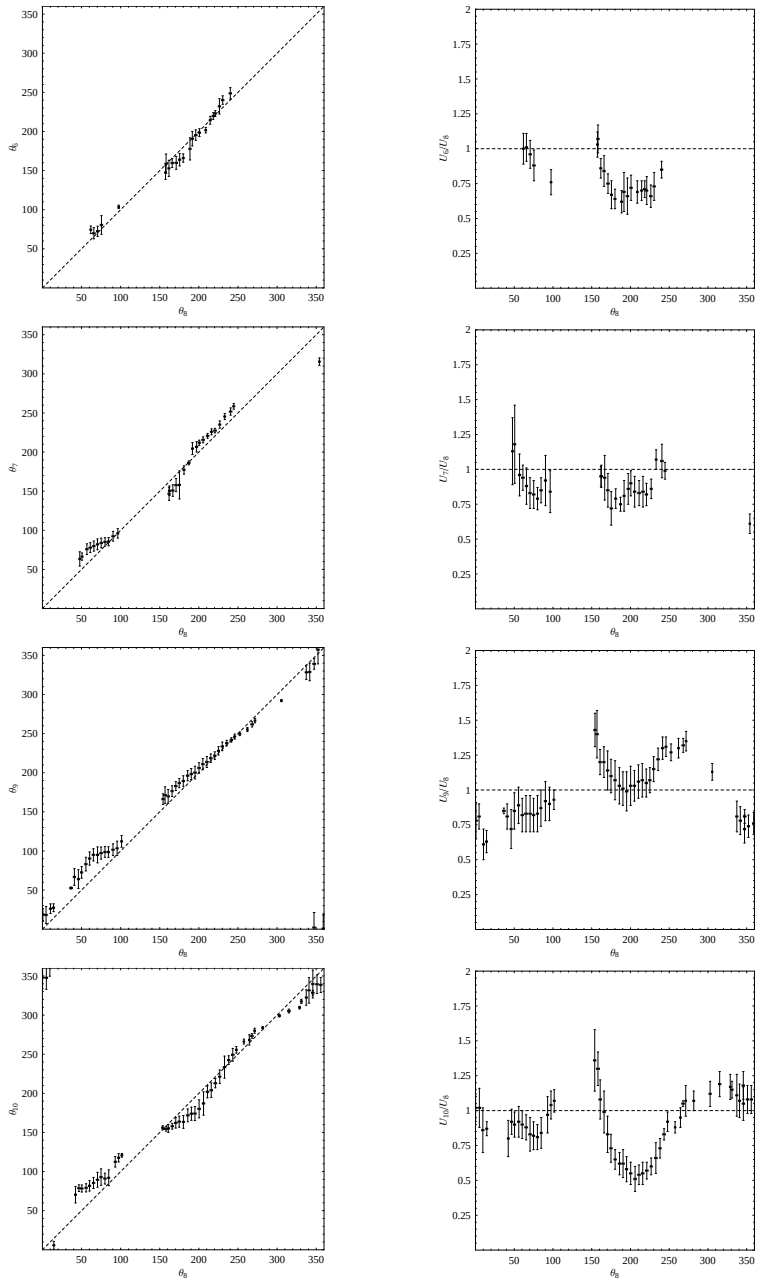

Figure 5. Analyzed wind directions and speed ratios.

by letting the wind speed tend to infinity, but in reality we are limited by the lack of data at very high wind speeds. We can get a rough idea of the effects of stability from the gust measurements. For large enough wind speeds we expect a constant value of the mean gust factor (gust wind to mean wind ration). Figure 6 shows an example, where a constant gust factor is reached at about 10 m/s. Plots for the other stations are very similar. The high gust factors at low wind speeds are probably a result of the turbulence induced by unstable conditions. Above 10 m/s the gust factor is almost constant with a slight tendency to decrease. The decrease can possibly be explained as an effect of the increase of the boundary layer height with the wind speed: mountain tops that reach up to near a capping inversion can excite gravity waves in the boundary layer which will tend to raise the gust factor at downwind positions. The standard deviation of the gust

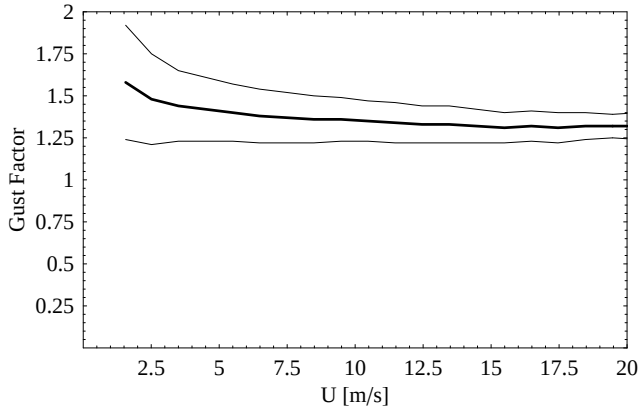

Figure 6. Mean gust factor vs. mean wind speed for Station 8. Thin lines indicate ± one standard deviation.

factor seems to continue to decrease even at the highest wind speeds. The reason for this is unclear but it might be the result of such effects. Judged from figure 6 it seems best to avoid wind speeds below 10 m/s. The highest wind speeds should be avoided too. Storms are associated with cyclones with winds circulating a low pressure, and streamlines are therefore likely to be curved during storms.

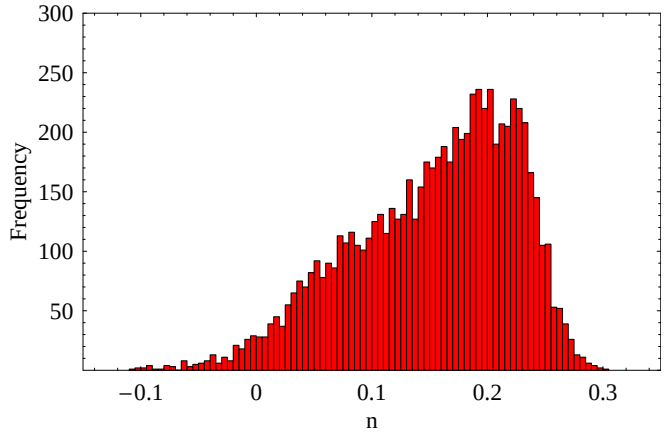

Figure 7. Histogram of n (see text) derived from NCEP/NCAR re-analysis data.

The NCEP/NCAR reanalysis database was used to derive further information on stability. The temperature profile may be parameterized by an exponent n so that

$$\frac{T_1}{T_2} = \left[\frac{P_1}{P_2}\right]^n \tag{7}$$

In a neutral, isentropic boundary layer we have

$$n = \frac{C_P - C_V}{C_P} \approx 0.286 \tag{8}$$

Lower values of n indicate a stable profile. Figure 7 shows a histogram of n obtained from temperatures at 1000 mb and 850 mb taken from the NCEP/NCAR re-analysis database. Evidently n is almost exclusively on the stable side. This may be due to the fact that 850 mb, corresponding to a height of approximately 1500 m, will often lie above a capping inversion. Therefore n is not a good indicator of stability, but temperatures at a lower level, say at 950 mb, or sensible heat fluxes are unfortunately not available. An attempt was made use a selection criterion on n, but it did no lead to any reduction of the scatter.

3 Computational method

Here we calculate the flow over the sites presented in the previous section and compare with the measurements.

3.1 Equations describing the basic flow problem

The governing differential equations for the problem of flow over complex terrain are the Navier-Stokes equations for an isotropic and incompressible fluid. A formulation in curvilinear coordinates is utilized.

Derivations related to the governing equations in curvilinear coordinates specific for the flow solver are given in Sørensen (1995). The basic principle was set forth by Vivand (1974). A general derivation based on tensor calculus is given in Jørgensen (2003). It is possible to solve the flow problem on a terrain following grid generated by a hyperbolic grid generator (see Sørensen (1998)). By Reynolds averaging we obtain the RANS equations

$$\sqrt{g}\frac{\partial}{\partial t}(\rho u^k)+\frac{\partial}{\partial \acute{x}^i}(\sqrt{g}\;\alpha^i_m \rho u^m u^k) = -\frac{\partial}{\partial \acute{x}^i}(\sqrt{g}\;\alpha^i_m g^{mk} p)+\sqrt{g}F^k$$
$$\frac{\partial}{\partial \acute{x}^i}\left(\sqrt{g}\;\alpha^i_m \alpha^j_n g^{kn}\mu\frac{\partial}{\partial \acute{x}^j}(u^m)+\sqrt{g}\;\alpha^i_m \alpha^j_n g^{mn}\mu\frac{\partial}{\partial \acute{x}^j}(u^k)\right) \tag{9}$$

where g^{mn} is the inverse of the fundamental tensor, g is the determinant of the transformed fundamental tensor, and where the transformation from the physical coordinates (x^i) to transformed coordinates $(\acute{x}^j)$ is given by

$$\acute{T}^j = \alpha^j_i T^i = \frac{\partial \acute{x}^j}{\partial x^i} T^i \tag{10}$$

Furthermore, the incompressible continuity equation is given by

$$\frac{\partial}{\partial \acute{x}^i}\left(\sqrt{g}\;\alpha^i_j u^j \rho\right) = 0 \tag{11}$$

In addition, to model the turbulence we applied the well-known $k-\varepsilon$ turbulence model described by the equations (denoting the turbulent kinetic energy by E)

$$\begin{aligned}\sqrt{g}\frac{\partial}{\partial t}(E)+\frac{\partial}{\partial \acute{x}^i}(\sqrt{g}\;\alpha^i_j u^j E) &= \frac{\partial}{\partial \acute{x}^i}\left(\sqrt{g}\;\frac{\nu}{\sigma_E}\alpha^i_m \alpha^j_n g^{mn}\frac{\partial}{\partial \acute{x}^j}(E)\right)\\ &\quad +\sqrt{g}\,\Pi-\sqrt{g}\,\varepsilon \end{aligned}\tag{12}$$

$$\begin{aligned}\sqrt{g}\frac{\partial}{\partial t}(\varepsilon)+\frac{\partial}{\partial \acute{x}^i}(\sqrt{g}\;\alpha^i_j u^j \varepsilon) &= \frac{\partial}{\partial \acute{x}^i}\left(\sqrt{g}\;\frac{\nu}{\sigma_\varepsilon}\alpha^i_m \alpha^j_n g^{mn}\frac{\partial}{\partial \acute{x}^j}(\varepsilon)\right)\\ &\quad +\sqrt{g}\,C_{\varepsilon 1}\frac{\varepsilon}{E}\Pi-\sqrt{g}\,C_{\varepsilon 2}\frac{\varepsilon}{E}\varepsilon \end{aligned}\tag{13}$$

where the turbulent kinematic viscosity is given by

$$\nu = C_\mu \frac{E^2}{\varepsilon} \tag{14}$$

and the production is given by

$$\Pi = \nu\left(\alpha^i_m \alpha^j_n g^{kn}\frac{\partial u^m}{\partial \acute{x}^j}+\alpha^i_m \alpha^j_n g^{mn}\frac{\partial u^k}{\partial \acute{x}^j}\right)\frac{\partial u^q}{\partial \acute{x}^i} g_{kq} \tag{15}$$

We used the in-house CFD solver EllipSys3D, which was developed jointly by Risø National Laboratory and the Technical University of Denmark, see Michelsen (1992), Michelsen (1994) and Sørensen (1995). The details of the implementation of EllipSys3D are given in Sørensen (1995).

3.2 Boundary conditions

The governing eqution of the flow problem are solved within a domain with six boundaries - inlet, outlet, lower, upper, left lateral and right lateral. The corresponding boundary conditions are given as below. Details of implementation can be found in Sørensen (1995). The normal derivative is denoted by $\partial/\partial n$.

Inlet boundary conditions

$$U^1 = \frac{U_\tau}{\kappa}\ln\frac{z}{z_0},\ U^2 = 0,\ U^3 = 0,\ \frac{\partial p}{\partial n} = \text{constant},\ E = \text{constant},\ \varepsilon = \frac{U_\tau^3}{\kappa\, z}.$$

Outlet boundary conditions

$$\frac{\partial U^1}{\partial n} = 0,\ \frac{\partial U^2}{\partial n} = 0,\ \frac{\partial U^3}{\partial n} = 0,\ \frac{\partial p}{\partial n} = \text{constant},\ \frac{\partial E}{\partial n} = 0,\ \frac{\partial \varepsilon}{\partial n} = 0$$

Lower boundary conditions

$$U^1(z_0) = 0,\ U^2(z_0) = 0,\ U^3(z_0) = 0,\ \frac{\partial p}{\partial n} = 0,\ \frac{\partial E}{\partial n} = 0,\ \varepsilon = C_\mu^{\frac{3}{4}}\frac{E^{\frac{3}{2}}}{\kappa\, z}$$

For the lower boundary conditions, modifications have been implemented in the momentum transport equations in order to match the surface shear stress with the law of the wall for the $k-\varepsilon$ model. Details are given in Sørensen (1995) where it is assumed that the surface shear stress is aligned with the velocity vector near the surface.

Upper boundary conditions

$$\frac{\partial U^1}{\partial n} = 0,\ \frac{\partial U^2}{\partial n} = 0,\ U^3 = 0,\ \frac{\partial p}{\partial n} = 0,\ \frac{\partial E}{\partial n} = 0,\ \frac{\partial \varepsilon}{\partial n} = 0$$

The upper boundary conditions are symmetry conditions.

Lateral boundary conditions

$$\frac{\partial U^1}{\partial n} = 0,\ U^2 = 0,\ \frac{\partial U^3}{\partial n} = 0,\ \frac{\partial p}{\partial n} = 0,\ \frac{\partial E}{\partial n} = 0,\ \frac{\partial \varepsilon}{\partial n} = 0$$

The lateral boundary conditions are symmetry conditions.

3.3 Generation of computational grids

In order to carry out a successful compuation of a flow field, one must be able to generate a grid which is suitable for an appropriate numerical representation of the important physical features of the flow problem. Model computations using the standard $k-\varepsilon$ model for atmospheric flow over flat terrain have been reported in the conference paper by Jørgensen, Hansen, Myllerup, Sørensen, Mann, Ott and Badger (2004). The discretization errors associated with grid cell sizes near the surface turns out to be by far the most important in contrast to the other effects. The effect of having too coarse grid cells near the bottom surface affects the wind speed far above typical inner layer heights. The inner layer height, l, is defined here as by N-O. Jensen (see Jensen, Petersen and Troen (1984)) via the expression

$$\frac{l}{\Delta x}\ln^2\left(\frac{l}{z_0}\right) = 2\kappa^2 \tag{16}$$

which can be solved by a transcendental procedure. Many other definitions exist, most of which yield larger values for l. At a distance, Δx downstream of a change of surface

momentum flux, we consider a region with constant momentum flux, i.e. constant U_τ. Within this region, the vertical mean velocity profile is logarithmic for heights below the inner layer height, l. It occurs in other literature related to CFD over terrain that bottom grid cells have heights comparable to the inner layer height. This is a practice which is a known from mesoscale modelling of atmospheric flows. However, at the micro scale, i.e. for CFD calculations over terrain, it has the consequence that grid independent solutions cannot be obtained.

Computational grids over complex terrain were generated by using 2D and 3D versions of the hyperbolic grid generation programs HypGrid2D/3D (Sørensen (1998)). Surface meshes over 3D terrain sites are based on files produced by a program developed by B. Broe and J. Mann, which is similar to the WAsP utility program map2grid. Based on a horizontal description of the grid point location (x,y), the surface grid generator performs interpolation in a series of gridded files to compute the height at each grid point location. It contains tools for modifying the terrain near the boundaries of the computational domain, and to align the computational grid with the intended flow direction.

3.4 Wind tunnel tests vs. atmospheric tests

An important aspect is the validation of the computed results against measurements. However, measurements in the atmosphere are expensive to perform. Usually, data are only obtained in a few points and only at very few heights. Moreover, the large scale flow around the test site cannot be controlled. Therefore, we utilized measured data from wind tunnel tests to perform a first validation.

We have set up atmospheric test cases for natural terrains based on measurement data from several measurement campaigns including flat, moderately complex and complex terrains. Model computations using the standard $k-\varepsilon$ model for atmospheric flow over flat terrain was reported in the conference paper by Jørgensen et al. (2004). In the present report, the focus is on the atmospheric test cases for complex terrain.

3.5 Model computations for the Hjardemål experiment

The forward and backward flows over the Hjardemål escarpment, Denmark, have been computed. The experimental data from an old but detailed measurement campaign performed by Risø was processed in order to facilitate comparison with computations. Previous work has been performed for the Hjardemål escarpment, see Jensen, Troen and Højholt (1990), which discuss model comparisons, and Emeis, Frank and Fiedler (1995) and Courtney, Højstrup and Jensen (1990) on the field study. Also, work has been reported about escarpments, for instance in Jensen (1983) and Jensen and Peterson (1978).

It is interesting that the first calculations with the CFD model did not agree very well with the measurements near the escarpment. Until it was realized that the transect of the applied orographic map did not agree with the measured cross section of the escarpment, a considerable effort was spent trying to change the roughness, turbulence parameters and grid resolution. Even a full 3D computation for the entire map was attempted, see Figure 8, but with nearly the same result as the previous calculations. Inspecting Figure 9 it is seen that an entire section at the top of the escarpment is shifted 30 m downstream compared to the measured orography. Also, the slope of the escarpment is different. In addition, a longer section upstream of the escarpment has a slightly wrong slope. Thus, it is an important conclusion that accurately measured orography must be available in order to do model calculations for complex terrain. This of course also applies for the simpler WAsP model.

The utilized computational grid was based on a surface produced by extraction of a measured 2D cross section of the escarpment and the nearby terrain. This cross section is shown as discrete symbols in Figure 9. Also, the line depicts a transect of a contour map that was initially used for the computations. The grid utilized $256 \times 64 \times 128$ cells cover-

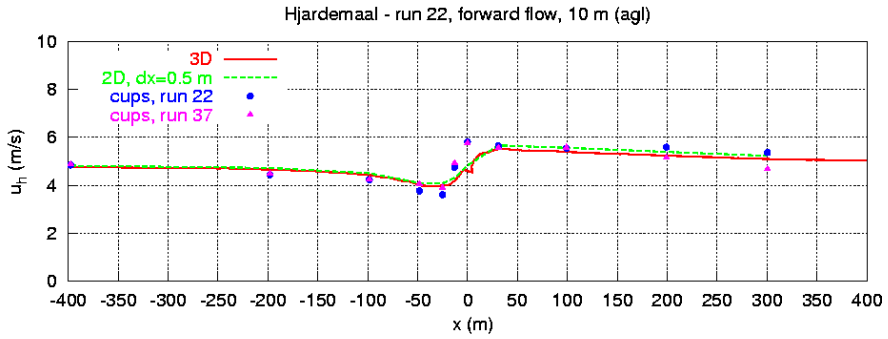

Figure 8. Forward flow over the Hjardemål escarpment. Wind speed of 2D and 3D model results based on a contour map from Kort and Matrikelstyrelsen compared against measurements.

ing $8000 \times 6400 \times 720\ m^3$. The reason for extracting the 2D cross section to a 3D grid was to test EllipSys3D before performing 3D computations on a more complex terrain. The

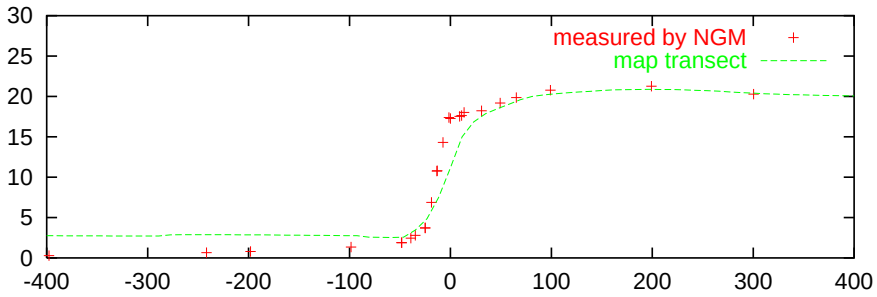

Figure 9. Measured profile (discrete symbols) versus a transect (line) of a contour map from Kort and Matrikelstyrelsen.

computations using the standard $k-\varepsilon$ model utilized a logarithmic inlet velocity profile

$$U = \frac{U_\tau}{\kappa} \ln \frac{z}{z_0} \tag{17}$$

matched to the upstream cup anemometer measurements. Also, the inlet turbulent kinetic energy and dissipation were adjusted to the turbulent kinetic energy measured upstream by sonic anemometers. The turbulence model parameters C_μ and $C_{\varepsilon 1}$, were adjusted following the procedure of Sørensen (1995). Hence,

$$C_\mu = \frac{U_\tau^4}{E^2} \tag{18}$$

$$C_{\varepsilon 1} = C_{\varepsilon 2} - \frac{\kappa^2}{C_\mu^{\frac{1}{2}} \sigma_\varepsilon} \tag{19}$$

The inlet dissipation was estimated via the expression

$$\varepsilon = \frac{U_\tau^3}{\kappa\, z} \tag{20}$$

The resulting parameters for the forward flow are shown in Table 2. The value calculated for $C_{\varepsilon 1}$ was 1.45. By a mistake the slightly smaller value $C_{\varepsilon 1} = 1.41$ was actually used for the forward flow case. However, such small changes in $C_{\varepsilon 1}$ seemed to have little effect in test calculations of the flow. For the forward case, the inlet profile matched the measured profile for the friction velocity $U_\tau = 0.33\ m/s$ with roughness $z_0 = 0.03\ m$. The measured

Table 2. Turbulence model parameters for Hjardemål, forward flow.

C_{mu}	$C_{\varepsilon 1}$	$C_{\varepsilon 2}$	σ_E	σ_ε	κ
0.07	1.41	1.92	1.00	1.30	0.40

inlet TKE was $E = 0.42\ m^2/s^2$. The estimated inlet dissipation was $\varepsilon = 0.09\ m^2/s^2$ for $\Delta z = 1.0\ m$.

The results for forward flow over the escarpment are shown in Figure 10. The plot shows the wind speed at 10 m height above terrain along the row of meteorological masts. The wind speed from two different runs of measurements are shown for comparison. Also shown are the results of the simpler WAsP model. Vertical profiles of wind speed are shown in Figure 11. The profiles should be read as reaching the value 0 when touching the terrain. At some height above the terrain, the corresponding wind speed is understood to be the difference between the values of the top axis for the given height and the height of the terrain. Again, the model results, the measurements and the results of the WAsP model are shown. It can be seen that in the forward flow case, the model wind speeds come close to the measured values. Also, there is little difference between the simpler WAsP model and the CFD model. However, the CFD model is more accurate near the top of the escarpment, although the difference is marginal. As a curiosity, the measuring point from run 22 at 25 m height indicates a wind speed 3 m/s larger than the corresponding measuring point from run 37, which matches the logarithmic inlet profile. A number of reasons for this could be stated. For instance, it could be the effect of an internal boundary layer which has not yet grown sufficiently at the upstream station. In this connection it should be considered, that the measuring point is actually an averaged value for a time interval within which external conditions might vary considerably because of large scale atmospheric structures passing through the measuring area. However, a likely reason is a measuring error during run 22. The modelled turbulent kinetic energy (TKE) plotted along the horizontal direction at 10 m height above the terrain is shown in Figure 12. Although expected to be difficult to model accurately, the modelled TKE is very similar to the sonics measurements. The sonics measure the three components of the Reynolds stress needed to compute the TKE. For the backward flow case, the inlet profile matched

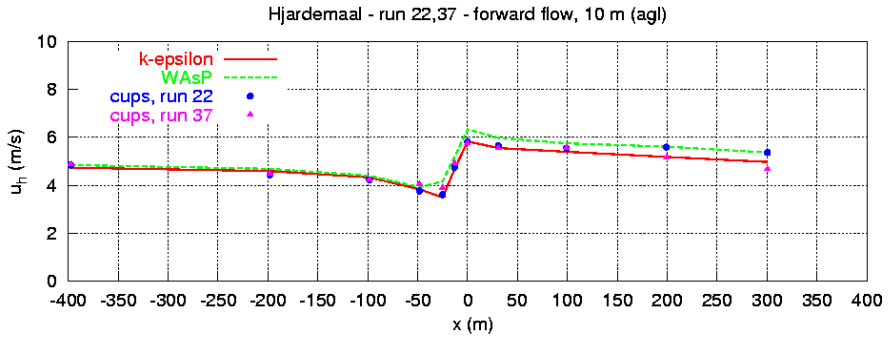

Figure 10. Forward flow over the Hjardemål escarpment. Computed model results versus measured wind speed. Also shown are the results of the WAsP calculations.

the measured profile for the friction velocity $U_\tau = 0.52\ m/s$ with roughness $z_0 = 0.03\ m$. The measured inlet TKE was $E = 1.05\ m^2/s^2$. The estimated inlet dissipation was $\varepsilon = 0.352\ m^2/s^2$ for $\Delta z = 1.0\ m$. The turbulence model parameters are shown in Table 3.

The results for backward flow over the escarpment are shown in Figure 13. The right side of the plot is now upstream and the left side of the plot is downstream. The plot

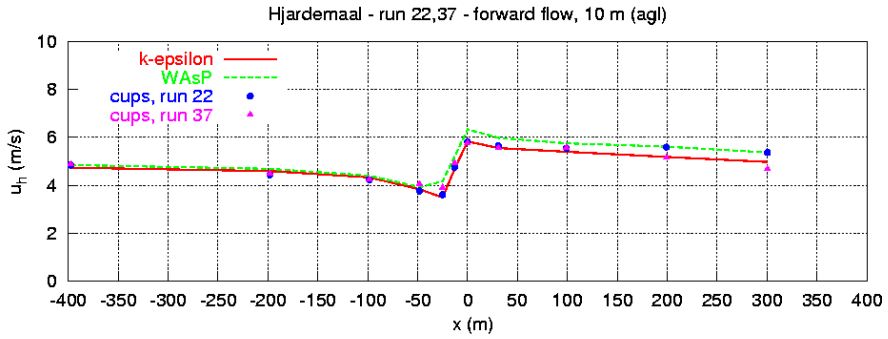

Figure 11. Vertical profiles of forward flow over the Hjardemål escarpment. Computed model results versus measured wind speed. Also shown are the results of the WAsP calculations.

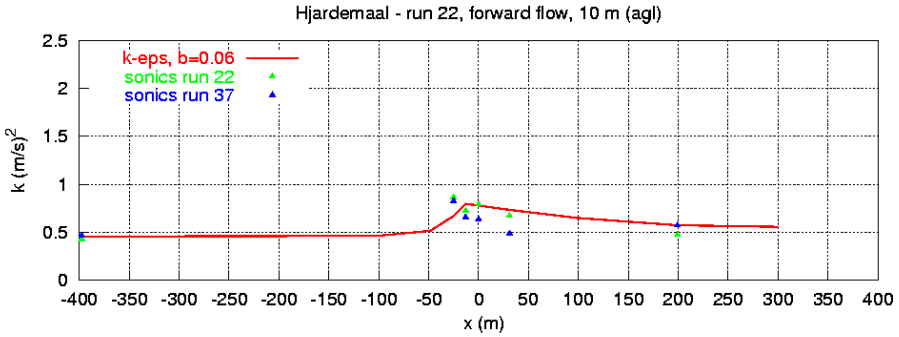

Figure 12. Forward flow over the Hjardemål escarpment. Model turbulent kinetic energy versus measurements.

shows the wind speed at 10m height above terrain along the row of meteorological masts. The wind speed from two different runs of measurements are shown for comparison. Also shown are the results of the simpler WAsP model. Vertical profiles of wind speed are shown in Figure 14. Again, the model results, the measurements and the results of the WAsP model are shown. It can be seen that in the backward flow case, that the wind speeds of the CFD model come close to the measured values. However, as the simpler WAsP gives the same response for forward and backward flow, there is large difference between the WAsP model and the CFD model - in particular near the escarpment. It is striking how well the wind speed profiles in the separated flow match the few measured data points. It would have been interesting to have measured data from several heights in this region. The modelled turbulent kinetic energy (TKE) plotted along the horizontal direction at 10 m height above the terrain is shown in Figure 15. Also shown are the sonics measurements. The sonics measure the three components of the Reynolds stress needed to compute the TKE. The modelled level of the TKE fits with the upstream measurements. In between the top of the escarpment (0 m) and 40 m upstream, the measured

Table 3. Turbulence model parameters for Hjardemål, backward flow.

C_{mu}	$C_{\varepsilon 1}$	$C_{\varepsilon 2}$	σ_E	σ_ε	κ
0.07	1.45	1.92	1.00	1.30	0.40

TKE increases while little change is predicted by the model. The downstream response in the modelled TKE is in agreement with the measurements. However, there are no measurements of TKE in between the bottom of the escarpment ($-30\ m$) and the next few hundred meters downstream. A likely explanation of the increase of TKE upstream of the top of the escarpment is the curvature of the terrain near the top of the escarpment. It is known that cavities in the surface (concave curvature) cause the release of TKE, see for instance Jensen (1983). As the gradient of TKE perpendicular to the surface is close to zero, the increased level of TKE persists further away from the surface. However, the induced pressure gradient near the surface is not accounted for in the momentum balance assumed in the boundary condition of the model. It assumes the law of the wall which in fact requires the horizontal pressure gradient to be zero. This might explain why the model does not predict any change in TKE upstream of the escarpment. At the point where the flow reaches the top of the escarpment, the measured TKE drops to the level predicted by the model. This can be explained by the convex curvature at the top of the escarpment causing the suppression of TKE. Once the flow has separated downstream, the concave curvature at the bottom of the escarpment causes a release of TKE. Hence the measured level of TKE increases near the surface in the separation zone, which is correctly predicted by the model. This is most likely due to the implementation in Ellip-Sys3D, where the law of the wall is matched with the surface shear stress in such a way that it is aligned with the velocity vector near the surface in order to accommodate the $k-\varepsilon$ model, see Sørensen (1995). The forward flow case is perhaps the most interesting

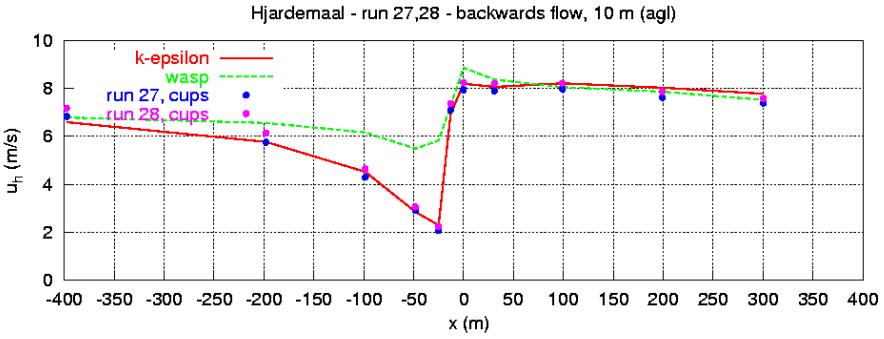

Figure 13. Backward flow over the Hjardemål escarpment. Computed model results versus measured wind speed. Also shown are the results of the WAsP calculations.

for wind energy purposes, because many wind turbines are erected on top of escarpments to benefit from the speed-up effect. However, when calculating the atmospheric flow over a more general complex terrain, there is typically many parts of the terrain which have steep slopes, some of which are backwards facing for common wind directions. Therefore, backward flow is important. Seen from the point of view of turbulence modelling, the backward flow case is interesting because the flow separation makes this case the most difficult to model. Even so, it is possible to model the wind speed accurately near the escarpment which has slope of approximately 30 degrees. A rule of thumb says that the simple models such as WAsP are not reliable beyond slopes of 30 degrees. However, it has been demonstrated that the CFD model equipped with a standard $k-\varepsilon$-model is capable of calculating the wind speed more accurate over steep slopes than the simpler WAsP model.

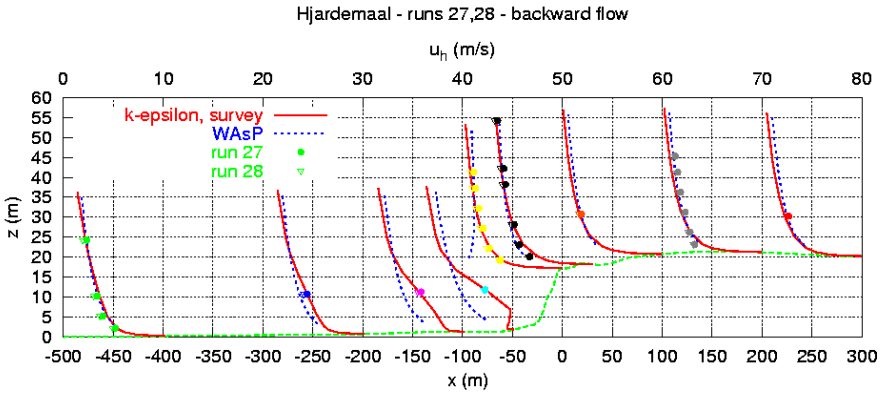

Figure 14. Vertical profiles of backward flow over the Hjardemål escarpment. Computed model results versus measured wind speed. Also shown are the results of the WAsP calculations.

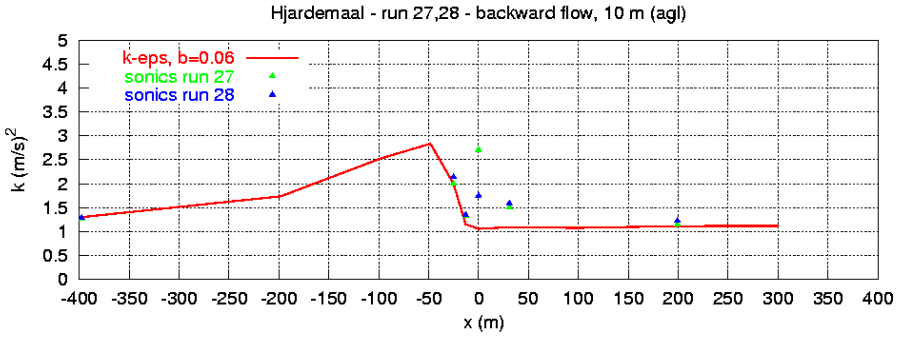

Figure 15. Backward flow over the Hjardemål escarpment. Model turbulent kinetic energy versus measurements.

Grid independence for Hjardemål

Grid independence has been tested by changing the vertical resolution near the surface and the horizontal resolution near the escarpment. The backward flow case is the most demanding (compared to the forward flow case). It requires a vertical resolution of 0.06 *m* near the surface. This scale is comparable to the roughness of 0.03 *m*. Plots for different vertical resolutions are shown for wind speed, see Figure 16, and Turbulent Kinetic Energy (TKE), see Figure 18. The required horizontal resolution is 2.0 *m* near the escarpment. Plots of different horizontal resolutions are shown for wind speed, see Figure 17, and TKE, see Figure 19. Note that the change in velocity and TKE is rather small when changing from the finest grid resolution to the next finest resolution, both for a vertical and a horizontal change. For a vertical resolution of 0.12 *m* near the surface, it was found that horizontal grid independence for TKE could not be achieved, even for horizontal resolutions down to 0.5 *m* near the escarpment. Thus, in order to alleviate this problem, the vertical resolution of 0.06 *m* near the surface was decided.

3.6 Conclusions for the Hjardemål computations

In conclusion there is a good agreement between measurements and computations for the Hjardemål experiment. Improvements in the computed Turbulent Kinetic Energy (TKE) might be obtained by implementing a different boundary condition for the TKE including

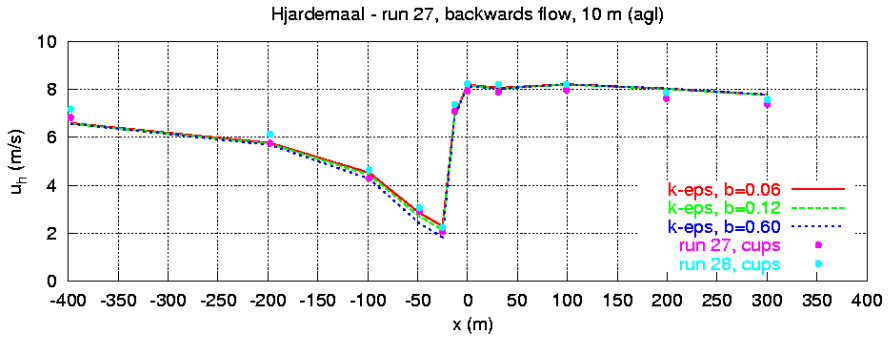

Figure 16. Backward flow over the Hjardemål escarpment. Computed model results for different vertical resolutions (near the surface) versus measured wind speed. The horizontal resolution is 2.0 *m near the escarpment.*

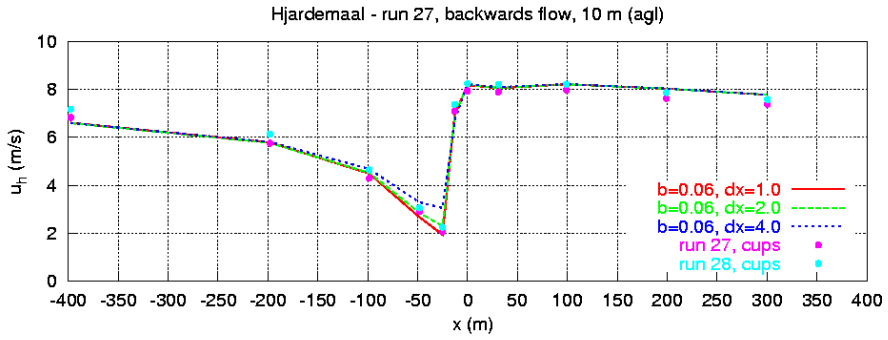

Figure 17. Backward flow over the Hjardemål escarpment. Computed model results for different horizontal resolutions (near the escarpment) versus measured wind speed. The vertical resolution is 0.06 *m near the surface.*

the pressure gradient near the surface. The measurements utilized plenty of instruments, thus making it possible to compare the development of the flow to the model results for evaluation of the model. However, more sonics could have been used in the zone

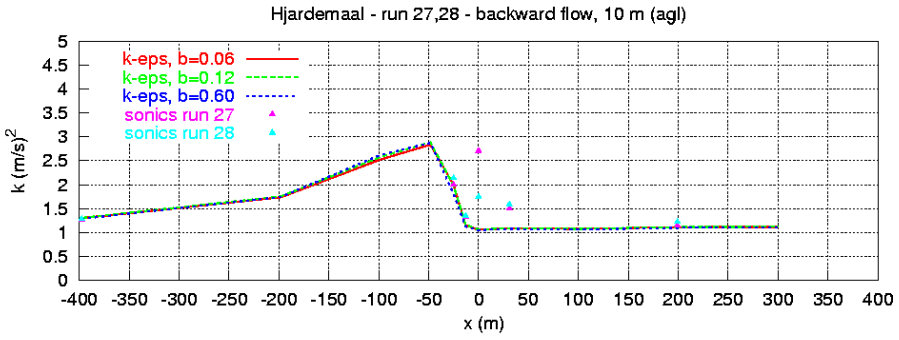

Figure 18. Backward flow over the Hjardemål escarpment. Computed model results for different vertical resolutions (near the surface) versus measured Turbulent Kinetic Energy (TKE). The horizontal resolution is 2.0 *m near the escarpment.*

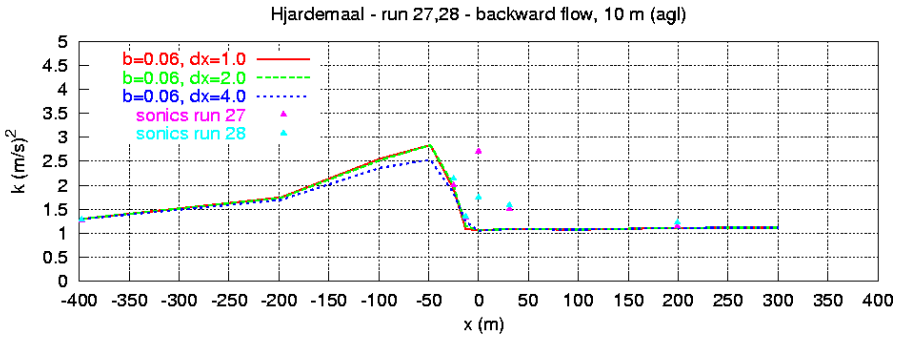

Figure 19. Backward flow over the Hjardemål escarpment. Computed model results for different horizontal resolutions (near the escarpment) versus measured Turbulent Kinetic Energy (TKE). The vertical resolution is 0.06 *m near the surface.*

in front of the escarpment in order to obtain the TKE for the backward flow. A similar experiment is suggested for a test site with a steeper slope. As the data for the Hjardemål experiment include cases affected by thermal stability, further work could be done by including a transport equation for heat in addition to buoyancy terms in the turbulence model equations. This would enable a study of model behavior under the influence of thermal stability.

3.7 Model computations for Porto

In order to test the use of the CFD model for a more complex site, Computations were performed of the flow over a site near Porto in northern Portugal. An overview of the meteorological stations is shown in Figure 20. It was desired to utilize a test case with the wind direction aligned with a row of meteorological masts, to see if any development in the wind field can be predicted by the model. Based on the data at hand and the position of the masts, a general wind direction of 220° was decided. This is because it is aligned with the row of the three masts, 6, 7, 8, and becuase more wind data was available for this direction than for the alternative directions. A grid aligned with the general flow direction was generated, covering a domain of 20 $km \times 12$ $km \times 5$ km, and containing $256 \times 256 \times 128$ cells. Horizontal stretching was applied to yield a resolution of 20 m near the stations. The first station, 8, is located 9 km downstream of the inlet. The first 4 km of the surface after the inlet were smoothed prior to the grid generation to yield a flat bottom at the inlet. This was to be able to provide suitable inlet conditions by using a logarithmic velocity inlet profile. The idea is to let the flow develop over the terrain before reaching the upstream meteorological station. Also, the last 3 km of the surface before the outlet were smoothed prior to the grid generation. This was to prevent zones with separating flow to extend through the outlet. In addition, the two outer zones consisting of the nearest 2 km of the surface before the lateral boundaries were smoothed. This was in order to prevent the generation of gradients in the flow conflicting with the symmetry conditions applied at the lateral boundaries. Horizontal stretching was kept below 7%. The bottom cell height was set to 0.20 m compared to a roughness length of 0.05 m. Although a roughness map existed, it was not large enough to cover the entire terrain of the computational domain. Also, differences existed among different roughness maps. Therefore, a constant roughness of 0.05 m was decided.

Instead of matching the inlet velotity profile to match the upstream station 8 exactly, the results are compared in the form of speedup, i.e. the ratio between the wind speed at a mast and the wind speed at the upstream station. Hence, the friction velocity of the inlet velocity profile was fixed at the value $U_\tau = 0.75\ m/s$, in order to yield wind speeds larger

than 10 m/s near the instruments. All the stations only had instruments mounted at 10 m agl. No turbulence data are available. For sufficiently large measured wind speeds, the flow is assumed to be near-neutral. For (stable and) neutral conditions (see Panofsky and Dutton (1984)) an assumption of flow over flat terrain yields a Turbulent Kinetic Energy (TKE) of

$$E = \frac{1}{2}\left(\sigma_u^2 + \sigma_v^2 + \sigma_w^2\right) = 5.466 U_\tau = 3.07 m^2/s^2 \tag{21}$$

This expression was used to estimate a suitable inlet TKE. The inlet dissipation was estimated via Eq. 20, i.e. $\varepsilon = 1.05 m^2/s^3$ for $\Delta z = 1.0\ m$. The turbulence model parameters C_μ and $C_{\varepsilon 1}$, were adjusted following the procedure of Sørensen (1995), using Eq. 18 and Eq. 19. The resulting turbulence model parameters are given in Table 5.

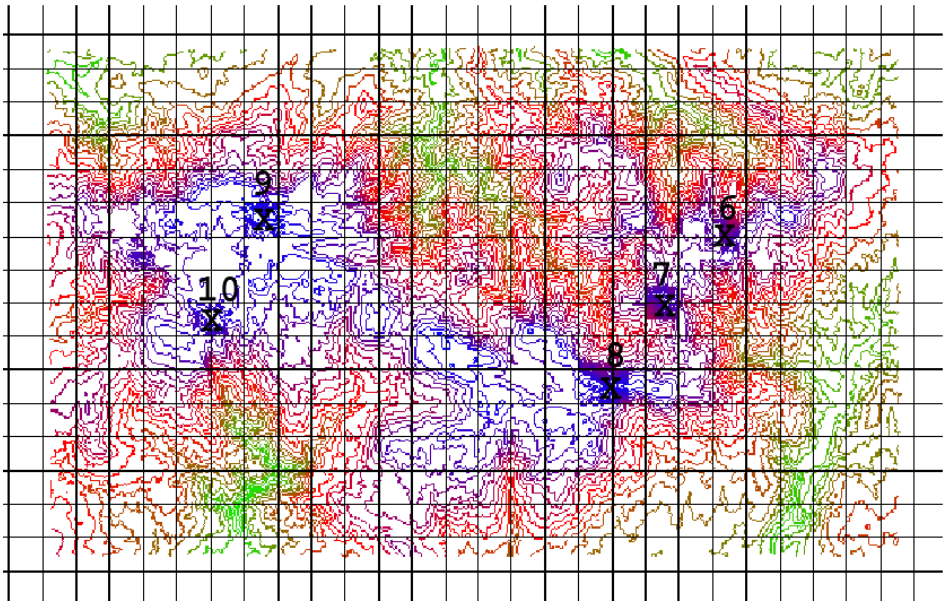

Figure 20. Overview of meteorological stations at the Porto site in Portugal. Each square is 1km × 1km. The shown contours are height contours. The zones near the stations have more densely distributed height contours, which has the appearance of small squares near each station.

Table 4. Station locations for Porto in UTM29 (WGS84) coordinates.

Station	Easting (m)	Northing (m)	Z (m)
6	577035	4524805	932
7	575487	4522871	982
8	573659	4520273	1057

Table 5. Turbulence model parameters for Hjardemål, forward flow.

C_{mu}	$C_{\varepsilon 1}$	$C_{\varepsilon 2}$	σ_E	σ_ε	κ
0.03	1.20	1.92	1.00	1.30	0.40

The results for the speedup are compared to the corresponding measured values in Table 6. It is seen that the model speedup has the same tendency as the measured speedup. However, the numbers don't match exactly, and not even within the estimated tolerance

for the measurements. The wind directions match for the stations 6 and 7. However, for the reference station, 8, there is a deviation of 12° between the modelled and the measured wind directions. This might be part of the explanation of the deviation between the modelled and the measured speedup for stations 6 and 7. It was decided not to spend time on more computations Porto with the purpose of checking grid dependence and investigating the effect of a number of refinements such as a detailed roughness map, sensitivity to changes of turbulence model parameters, changes of general wind direction etc. The reason is the lack of suitability of the measurement data to be used for model verification. The distance between the nearest meteorological stations is approximately 3 *km*, rendering little correlation among the stations with respect to the measured wind because of the complexity of the terrain. Only a few masts are aligned in a row, and they are only equipped with instruments at 10 *m* height agl. This makes it difficult to evaluate any development in the flow for model evaluation. There are no turbulence data available - in particular there are no upstream turbulence data available. The accuracy of the orographical map is unknown, and also the zones with increased level of near the stations are rather small.

Table 6. Computed speedup for Porto compared to measured speedup. The speedup is denoted by S. Also shown are wind directions, DD, and standard deviations σ.

Station	U_{hor} (m/s)	S model	DD (°)	S meas.	σ	DD (°)	σ
6	14.58	0.87	223	0.70	0.1	222	4
7	16.43	0.98	225	0.80	0.1	227	3
8	16.78	1.00	208	1.00	0.0	220	0

3.8 Conclusions for the Porto computations

It is very difficult to draw any conclusions about the model performance for Porto. This would require a new measuring campaign employing more masts and also more closely spaced masts, more instruments, including sonics, placed at several heights for at least some of the masts, a more detailed orographical map, especially in the zones near the meteorological stations, and a detailed roughness map covering the entire terrain of the computational area.

Acknowledgements

This work has been supported by STVF under the contract 26-02-0015. Furthermore, the work has been supported by the Danish Center for Scientific Computing (DCSC). The authors gratefully acknowledge these opportunities. Thanks to Jess A. Michelsen for developing the basis2d/3d platform and parallelized multigrid solver and building the Yggdrasil cluster. Thanks to Jørgen Højstrup for providing us with the measurement data of the Hjardemål experiment and many discussions. Thanks to Morten Nielsen and Peter Sanderhoff for technical assistance during the data archeological recovery efforts for Hjardemål. Thanks to Niels-Otto Jensen for providing helpful insight, photographs, papers about the Hjardemål experiment. Thanks to Søren E. Larsen for helpful advice and encouragement. Thanks to our friends and colleagues in the Department of Mechanical Engineering Department (MEK) at DTU for their help during the preparation of this document.

References

Ayotte, K. W., Davy, R. J. and Coppin, P. A.: 2001, A simple temporal and spatial analysis of flow in complex terrain in the context of wind energy modelling, *Boundary-Layer Meteorol.* **98**, 275–295.

Bechmann, A.: 2007, *Large-Eddy Simulation of Atmospheric Flow over Complex Terrain*, PhD thesis, Risø National Laboratory.

Castro, F. A., Palma, J. M. L. M. and Lopes, S.: 2003, Simulation of the Askervein flow. Part 1: Reynolds Averaged Navier-Stokes equations ($k-\varepsilon$ turbulence model), *Boundary-Layer Meteorol.* **107**, 501–530.

Courtney, M., Højstrup, J. and Jensen, N. O.: 1990, A field study of flow over an escarpment, *Ninth symposium on turbulence and diffusion*, AMS, Risø, Roskilde Denmark, pp. 363–366.

Emeis, S., Courtney, M. S., Højstrup, J. and Jensen, N. O.: 1993, Hjardemål experiment data report, *Technical Report Risø–M–2289(EN) /SFB 210/E/77*, Risø National Laboratory, Denmark.

Emeis, S., Frank, H. P. and Fiedler, F.: 1995, Modification of air flow over an escarpment - results from the hjardemål experiment, *Boundary-Layer Meteorol.* **74**, 131–161.

Högström, U., Hunt, J. R. C. and Smedman, A.-S.: 2002, Theory and measurements for turbulence spectra and variance in the atmospheric neutral surface layers, *Boundary Layer Meteorology* **103**, 101–124.

Hunt, J. R. C. and Morrison, J. M.: 2000, Eddy structure in turbulent boundary layers, *Eur. J. Mech.–Fluids* **19**, 673–694.

Jensen, N. O.: 1983, Escarpment induced flow pertubations, a comparison of measurements and theory, *J. Wind Eng. Ind. Aerodyn.* **15**, 243–251.

Jensen, N. O., Petersen, E. L. and Troen, I.: 1984, Extrapolation of mean wind statistics with a special regard to wind energy application, *Technical Report WCP-86*, World Meteorological Organization.

Jensen, N. O. and Peterson, E. W.: 1978, On the escarpment wind profile, *Q. J. R. Meteorol. Soc.* **104**, 719–728.

Jensen, N. O., Troen, I. and Højholt, P.: 1990, Model comparisons with flow over an escarpment, *Ninth symposium on turbulence and diffusion*, AMS, Risø, Roskilde Denmark, pp. 413–416.

Jørgensen, B. H.: 2003, Tensor formulation of the model equations on strong conservation form for an incompressible flow in general coordinates, *Technical Report Risø-R-1445(EN)*, Risø National Laboratory, Denmark.

Jørgensen, B. H., Hansen, A. D., Myllerup, L., Sørensen, N. N., Mann, J., Ott, S. and Badger, J.: 2004, Computational wind power meteorology in complex terrain compared to measurements, *2004 European Wind Energy Conference and Exhibition*, EWEA, London (GB), p. 7.

Kim, H. G. and Patel, V. C.: 2000, Test of turbulence models for wind flow over terrain with separation and recirculation, *Boundary-Layer Meteorol.* **94**, 5–21.

Michelsen, J. A.: 1992, Basis3D - a platform for development of multiblock PDE solvers, *Technical Report AFM 92-05*, Technical University of Denmark.

Michelsen, J. A.: 1994, Block structured multigrid solution of 2D and 3D elliptic PDE's, *Technical Report AFM 94-06*, Technical University of Denmark.

Panofsky, H. and Dutton, J. A.: 1984, *Atmospheric Turbulence: Models and Methods for Engineers and Scientists*, John Wiley and Sons.

Sørensen, N. N.: 1995, *General Purpose Flow Solver Applied to Flow over Hills*, PhD thesis, Risø National Laboratory, Denmark.

Sørensen, N. N.: 1998, HypGrid2D a 2-d mesh generator, *Technical Report Risø–R–1035(EN)*, Risø National Laboratory, Denmark.

Taylor, P. A. and Teunissen, H. W.: 1987, The askervein hill project: Overview and background data, *Boundary-Layer Meteorol.* **39**, 15–39.

Vivand, H.: 1974, Formes conservatives des équations de la dynamique des gaz, *Rech. Aérosp.* **1**, 65–66.

Walmsley, J. L. and Taylor, P. A.: 1996, Boundary-layer flow over topography: Impacts of the Askervein study, *Boundary-Layer Meteorol.* **78**, 291–320.

Risø's research is aimed at solving concrete problems in the society.

Research targets are set through continuous dialogue with business, the political system and researchers.

The effects of our research are sustainable energy supply and new technology for the health sector.